Letter

Optimal quantum reservoir computing for the noisy intermediate-scale quantum era

L. Domingo [1,2,3,*] G. Carlo,[4,†] and F. Borondo [1,2,‡]

[1]*Instituto de Ciencias Matemáticas, Campus de Cantoblanco, Nicolás Cabrera, 13-15, 28049 Madrid, Spain*

[2]*Departamento de Química, Universidad Autónoma de Madrid, Cantoblanco 28049 Madrid, Spain*

[3]*Grupo de Sistemas Complejos, Universidad Politécnica de Madrid, 28035 Madrid, Spain*

[4]*Comisión Nacional de Energía Atómica, CONICET, Departamento de Física, Av. del Libertador 8250, 1429 Buenos Aires, Argentina*

(Received 20 May 2022; revised 27 August 2022; accepted 19 September 2022; published 13 October 2022)

Universal fault-tolerant quantum computers require millions of qubits with low error rates. Since this technology is years ahead, noisy intermediate-scale quantum (NISQ) computation is receiving tremendous interest. In this setup, quantum reservoir computing is a relevant machine learning algorithm. Its simplicity of training and implementation allows to perform challenging computations on today's available machines. In this Letter, we provide a criterion to select optimal quantum reservoirs, requiring few and simple gates. Our findings demonstrate that they render better results than other commonly used models with significantly less gates and also provide insight on the theoretical gap between quantum reservoir computing and the theory of quantum states' complexity.

DOI: 10.1103/PhysRevE.106.L043301

Introduction. Pursuing the early idea of Manin [1] and Feynman [2] of constructing quantum computers that can solve numerical problems exponentially faster than the classical ones, some years ago Google and NASA claimed [3], not without controversy [4,5], having achieved this quantum supremacy. Although a universal fault-tolerant quantum computer [6] or efficient real-time error correction [7] could potentially solve hard benchmark challenging problems, such as integer factorization (the Shor algorithm [8]) or unstructured search (Grover's search [9]), and open new perspectives in the applications in many fields [10], such as quantum chemistry [11] or material science [12], such devices are still decades away from being realized. Interestingly enough, this fragility has not decreased the interest in quantum computing, but triggered a tremendous activity in the alternative called the *noisy intermediate-scale quantum* (NISQ) era [13], where quantum algorithms are developed to reach quantum advantage using the (small) quantum computers available today [14].

A highly relevant NISQ algorithm is *quantum reservoir computing (QRC)* [15,16] because of its suitability for implementation on NISQ devices. QRC has been demonstrated to excel not only in classical, but also quantum machine learning (QML) tasks. It exploits the quantum properties of physical systems and provides an easy training strategy, achieving excellent results [17]. QRC has most often been used in time predictions [18,19], using the memory of the reservoir for the task, but quantum reservoirs (QR) have also been used for nontemporal tasks, and then the terms QRC [20], quantum reservoir processing [16], and quantum extreme learning machines [17] are used to describe the QML algorithm. In this work, we will use the term QRC to refer to QML models which use QR, regardless of the QML task. Nevertheless, our approach can be extended for memory-requiring tasks and we defer this study to a future work. In gate-based quantum computation, QRC consists of a random quantum circuit applied to an initial state, which encodes the input data and the goal is to extract valuable information from the input state, so that the measurements of simple local operators are useful features to predict the output. These features are then fed to a classical machine learning algorithm, typically a linear model. The quantum reservoir must be a complex quantum circuit, so that the extracted features contain enough information for learning the output. Accordingly, the design of the QR is crucial for the performance of the model, so that selecting optimal QRs is of vital importance. In this respect, the *majorization principle* [21] has proven to be a superb indicator of the complexity of random quantum circuits [22]. Compared to other complexity criteria, such as the entanglement spectrum, evaluating the majorization in a quantum circuit requires significantly less operations. This makes the majorization principle a criterion *especially* suitable for the NISQ era, where quantum computation has to be performed with limited quantum resources. These limited resources include constraints not only in the size but also regarding the architecture of state-of-the-art quantum processors. In particular, the performance of a quantum algorithm is highly influenced by the quality of the quantum gates and the presence of noise. Our criterion also directly applies to these qualitatively different technological challenges given that it relies on a global statistical measure rather than on circuit-specific proofs. The great relevance of introducing this measure of complexity in the QRC realm is not limited to providing an extremely efficient way of selecting the optimal QR, but it also bridges the theoretical gap between QRC and the theory of the quantum states' complexity [23]. As a

*laia.domingo@icmat.es

†carlo@tandar.cnea.gov.ar

‡f.borondo@uam.es

matter of fact, here we introduce a quantitative classification of these algorithms with the growth of the quantum circuits' complexity that can be interpreted as the unitaries accessible dimension.

In this Letter, we use the majorization criterion to design the optimal QR in terms of performance for QML. The resulting quantum circuits are easily realized in NISQ [14] computers and present a significant advantage over the commonly used Ising model. The performance of QRC is assessed using different families of quantum circuits, which have different complexity according to the majorization principle. Also, we study the number of gates needed for each family to obtain optimal performance. In NISQ devices, this number should be as small as possible to minimize error propagation due to large error rates and short coherence times [14]. The results of our work show that the optimal quantum circuits provided in this work require significantly less quantum gates than the Ising model, which has been widely used as a QR [15,16,19,20]. The optimality of the QR is illustrated by solving a quantum chemistry problem. In this context, the data used to train the QRC model is already a quantum state. Therefore, it is natural to use a QML algorithm to infer the properties of the system. Moreover, to represent a quantum system with d degrees of freedom (d qubits), one would need a classical vector of size 2^d. In an actual quantum device, only d physical qubits are needed to encode the system state. NISQ devices can currently work with around 100 qubits, which classically would require using vectors of a size of the order of 2^{100} (given that not all of the Hilbert space can be used in NISQ devices), which are totally intractable. In this case, the machine learning task is to predict the energy of the excited states of a molecule, given its ground state, as presented in Ref. [20]. Such a ground state can be obtained as an output of another NISQ quantum algorithm, such as the variational quantum eigensolver (VQE) [24]. This task is relevant since computing the excited states of a Hamiltonian is a much more difficult task than computing its ground state.

Method. The majorization method can be summarized as follows. Let $x, y \in \mathbb{R}^n$ be probability vectors, i.e., real vectors of nonnegative components and normalized to unity. We say that y majorizes x ($x \prec y$) if for all $k < N$

$$\sum_{i=1}^{k} x_i^{\downarrow} < \sum_{i=1}^{k} y_i^{\downarrow}, \quad \sum_{i=1}^{N} x_i^{\downarrow} = \sum_{i=1}^{N} y_i^{\downarrow}, \tag{1}$$

where $x^{\downarrow}$ indicates that the vector was arranged in a nonincreasing order. The partial sums are called cumulants. In Ref. [22], the authors created random circuits and evaluated the final state in the computational basis, obtaining the associated probabilities x_M, where M is the number of gates of the circuit. This calculation was repeated for an increasing number of gates M and the cumulants calculated for each x_M. The results showed that the fluctuations (standard deviation) of all the cumulants for a given family of random circuits are a measure of the complexity of a quantum circuit. In this work, we consider seven *families* of quantum circuits, which have different complexity according to the majorization principle [22]. For a given family, the quantum circuit is done by adding random quantum gates from such a family. We perform 400 simulations for each type of quantum circuit. The seven families considered are the following. The first three circuits are constructed from a few generators: $G1 = \{\text{CNOT}, H, X\}$, $G2 = \{\text{CNOT}, H, S\}$, and $G3 = \{\text{CNOT}, H, T\}$, where CNOT is the controlled-NOT gate, H stands for Hadamard, and S and T are $\pi/4$ and $\pi/8$ phase gates, respectively. The circuits constructed from $G2$ generate the Clifford group [25] and $G1$ generate a subgroup of Clifford [26]. Therefore, both $G1$ and $G2$ are nonuniversal and classically simulatable. On the other hand, $G3$ is universal and thus approximates the full unitary group $U(N)$ to arbitrary precision. The fourth family is composed of matchgates (MG), which are two-qubit gates formed from two one-qubit gates, A and B, with the same determinant. A acts on the subspace spanned by $|00\rangle$ and $|11\rangle$, while B acts on the subspace spanned by $|01\rangle$ and $|10\rangle$. A and B are randomly sampled from the unitary group U(2). Matchgates circuits are also universal (except when acting on nearest-neighbor lines only) [27,28]. The last families of gates are diagonal in the computational basis. As diagonal gates commute, they can be applied simultaneously. We separate the diagonal gates into three families: D2, D3, and Dn. Here, D2 gates are applied to pairs of qubits, D3 gates are applied to three qubits, and Dn gates are applied to all the qubits. The diagonal D2, D3, and Dn families contain $\binom{n}{2}$, $\binom{n}{3}$, and 1 gates, respectively. Diagonal circuits cannot perform universal computation, but they are not always classically simulatable [29].

With these seven families of gates, quantum circuits suitable as QRs can be designed. Apart from the type of gates used, circuits are also characterized by a different *number* of gates. For the $G1$, $G2$, $G3$, and MG families, we construct circuits of 20, 50, 100, 150, and 200 gates and assess the influence of the number of gates in the final performance of the model. For the $G3$ family, we also construct circuits with up to 1000 gates, and with the matchgates we construct circuits with 5, 10, and 15 gates. The diagonal circuits have a fixed number of gates, so we only consider that number of gates for these circuits. Additionally, we compare the studied families with the Ising model. In this case, the quantum circuit performs the time evolution of a quantum state under the random transverse-field Ising Hamiltonian

$$H_{\text{Ising}} = \sum_{i,j=0}^{N-1} J_{ij} Z_i Z_j + \sum_{i}^{N-1} h_i X_i, \tag{2}$$

where X_i and Z_j are Pauli operators acting on the site i, jth qubit, and the coefficients h_i and J_{ij} are sampled from the Gaussian distributions $N(1, 0.1)$ and $N(0.75, 0.1)$, respectively. All time evolutions will be performed for a lapse of time $T = 10$. The parameters are chosen in the same way as in Ref. [20] for better comparison. In addition, we evaluated a different set of parameters according to Ref. [30], which provide a state-of-the-art method to select optimal parameters of the Ising model for QRC. In this case, J_{ij} are sampled from the uniform distribution $U(-J_s/2, J_s/2)$ and $h_i = h$ are constant. The optimal parameters in Ref. [30] fulfill $h/J_s = 0.1$. As an illustration, we choose to study the electronic ground and first excited states of two molecules, LiH and H_2O in the configuration ranges: $R_{\text{LiH}} \in [0.5, 3.5]$ a.u., $R_{\text{OH}} \in [0.5, 1.5]$ a.u., and $\phi_{\text{HOH}} = 104.45^{\circ}$. The corresponding electronic Hamiltonian and wave functions are denoted as $H(\vec{R})$, $\psi_0(\vec{R})$, and $\psi_1(\vec{R})$,

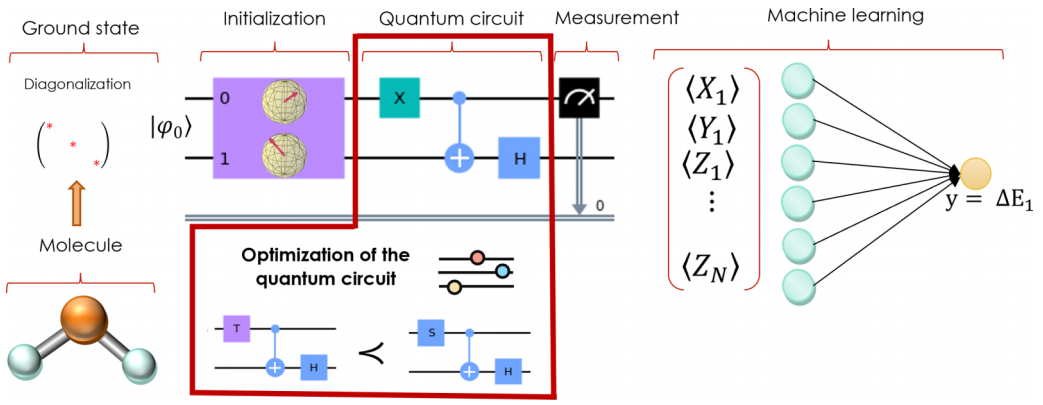

FIG. 1. Pipeline used to train the quantum reservoir computing model. First, the electronic Hamiltonian of the molecule is mapped to the qubit space and its ground state is calculated by direct diagonalization. Such a ground state is fed to the quantum reservoir, which is a random quantum system sampled from one of the seven families studied in this work. Local Pauli operators are then measured and fed to the classical machine learning algorithm, which predicts the excited energy of the molecule. The choice of the quantum reservoir is optimized according to the majorization principle introduced in Ref. [22].

respectively. The first step is to obtain the ground state of $H(\vec{R})$ in the qubit space. To do so, we calculate the second quantization Hamiltonian using the standard STO-3G basis for the Hartree-Fock optimization [11,31]. To use as few qubits as possible, we remove from the basis set the spin orbitals which are very likely to be either occupied or virtual in all Slater determinants in the wave function. In particular, the spin orbitals with a natural orbital occupation number close to 0 or 1 are assumed empty or occupied, respectively [11]. The second-quantized Hamiltonian is then mapped to the qubit space by using the Jordan-Wigner transformation [32]. More details about this process are given in the Supplemental Material (SM) [33]. Once the qubit Hamiltonian has been calculated, the corresponding ground state $|\psi_0\rangle_{\vec{R}}$ is calculated by (numerical) exact diagonalization. Then, we predict, using the QML algorithm, the target function

$$\Delta E(\vec{R}) = E_1(\vec{R}) - E_0(\vec{R}), \tag{3}$$

where $E_0(\vec{R})$ and $E_1(\vec{R})$ are the ground state and first excited energies, respectively. In this way, we obtain an eight-qubit ground state for LiH and a ten-qubit ground state for H_2O. We use different configurations of the molecules (i.e., different bond lengths and angles $\vec{R}$) to train the QML, which aims to predict the corresponding relative excited energy $\Delta E(\vec{R})$ for a given configuration $\vec{R}$. Then, we ask the QML algorithm to predict $\Delta E(\vec{R})$ for *new* values of $\vec{R}$. For the numerical simulation we split the data set $\{|\psi_0\rangle_{\vec{R}}, \Delta E(\vec{R})\}_R$ in training and test sets. The test sets contain 30% of the data, $R_{\mathrm{LiH}} \in [1.1, 2.0]$ a.u. and $R_{\mathrm{OH}} \in [1.05, 1.35]$ a.u. and it are chosen so that the reservoir has to extrapolate to unseen data.

Once we generate the training and test data, we design the pipeline of the QRC model, which is schematically shown in Fig. 1. The input of the QR, which is a quantum circuit with gates sampled randomly from one of the seven gate families described above, is $|\psi_0\rangle_{\vec{R}}$. For each experiment the random quantum circuit is the same for all values of R_{OH} or R_{LiH}. After applying the random circuit to the initial state, we measure the expectation values of the local Pauli operators $\{X_0, Y_0, Z_0, \ldots, X_n, Y_n, Z_n\}$, where X_i, Y_i, Z_i are the Pauli operators X, Y, Z applied to the ith qubit. Notice that since the Pauli operators $X_1, \ldots, X_n$ (similarly for $Y_1, \ldots, Y_n$ and $Z_1, \ldots, Z_n$) commute with one another, the associated observables can be simultaneously measured. Therefore, the number of experiments needed to obtain all the observed values does not scale with the number of qubits. The measurements provide a classical vector $X(\vec{R})$ containing the extracted information from the ground state

$$X(\vec{R}) = (\langle X_0\rangle, \langle Y_0\rangle, \langle Z_0\rangle, \ldots, \langle X_n\rangle, \langle Y_n\rangle, \langle Z_n\rangle)^T, \tag{4}$$

where n is the number of qubits and the expectation values are taken over the output state of the circuit $|\psi\rangle_{\vec{R}}$. This classical vector is then fed to a classical machine learning model. In this work we use the ridge regression, a regularized linear model which minimizes the mean squared error

$$\mathrm{MSE}_R = \frac{1}{N_s}\sum_{i=0}^{N_s}[W \cdot X(\vec{R}_i) - \Delta E(\vec{R}_i)]^2 + \alpha||W||^2, \tag{5}$$

where N_s is the number of samples in the training set, W is the matrix of the linear model, α is the regularization parameter, and $||\cdot||$ is the L^2 norm. Notice that, since the linear model has to extrapolate to unseen data (unseen values of $\vec{R}$), it is necessary to add regularization to the learning algorithm to prevent overfitting the training data. In this work we choose $\alpha = 10^{-7}$, a value that simultaneously prevents overfitting and provides accurate predictions. Although it is true that any other classical machine learning algorithm could have been used instead of this linear model, at this point the QR is able to extract valuable information from the quantum state. Thus, a simple machine learning model, like the one we are using here, is plenty enough to predict the excited properties of the system.

Results. Figure 2 shows the performance of QRC for the seven families of quantum circuits as a function of the number of gates of the circuits. Solid lines correspond to the LiH molecule and dashed lines to H_2O. As can be seen, the performance of the different circuits is qualitatively the same in both cases. In Fig. 3 of Ref. [22], it is seen how the fluctuations of the Lorentz curves differentiate the various families of random circuits, with the families with lower fluctuations

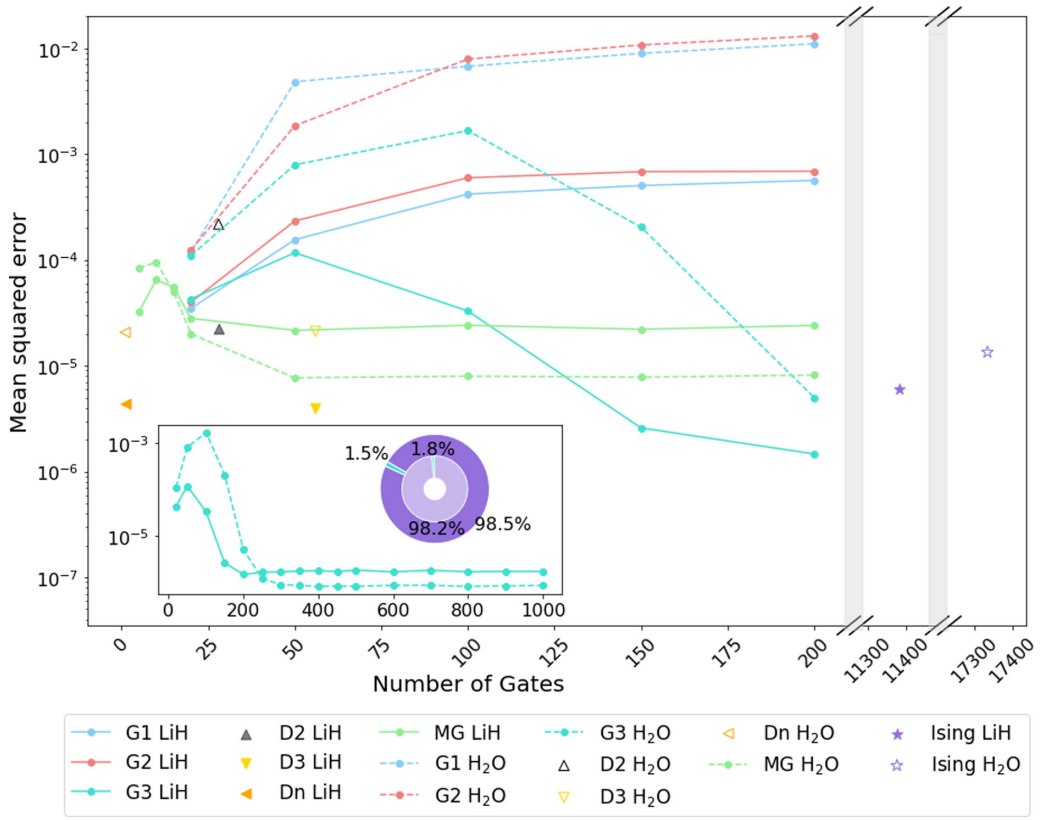

FIG. 2. Average mean squared error (MSE) of the seven families of quantum reservoirs as a function of the number of gates of the circuit. Averages are made over 400 simulations. The solid and dashed lines represent the results for the LiH and H_2O molecules, respectively. The plot also displays, for comparison, the average performance of the Ising model. The inset contains the MSE of the G3 circuits for larger number of gates. The pie charts represents the proportion of gates needed to obtain optimal performance for the G3 family and the Ising model.

closer to the Haar measure behavior corresponding to more complex random quantum circuits. Our results in Fig. 2 agree with the classification given in Ref. [22]. Circuits with higher complexity have a better performance in the QML task. In particular, the $G1$ and $G2$ families are the less complex families according to the majorization indicator, and they also give worse results in the QML task. On the other hand, the circuits in the $G3$ family give the lowest error in the predictions, which agrees with the $G3$ family having the highest complexity. The matchgates' circuits, on the other hand, have a slightly worse performance than the $G3$ family, which also agrees with the majorization criterion. Finally, the performances of the D3 and Dn circuits are very similar to each other, although the performance of the D2 circuits is significantly worse. This difference between the diagonal circuits is also seen when using the majorization indicator. Figure 2 also shows how the performance of the QML task changes with the number of gates of the circuit. The $G1$ and $G2$ circuits give worse results as the number of gates increase. On the contrary, the $G3$ circuits improve their performance with the number of gates, and this performance stabilizes around 200 gates for LiH, and around 250 for H_2O. The matchgate circuits also improve its performance with the number of gates, but in this case the optimal performance is achieved with only 20 gates (LiH) or 50 gates (H_2O), even though this optimal error is higher than the optimal error of $G3$. Notice that the H_2O system is larger (ten qubits) than for the LiH system (eight qubits). Therefore, predicting the excited energy $E_1(\vec{R})$ for the H_2O is a harder task, and it is expected that the optimal circuit requires more gates. The same analysis was performed to predict the second excited energy $E_2(\vec{R})$ for the two molecules under study. The results are qualitatively the same and are provided in the SM [33].

To further understand the difference in the performance of the circuits, we inspect how each of the random circuits span the space of operators. For simplicity and easier visualization we create a toy model of two qubits and apply random circuits from each of the families. Each of the circuits is a unitary operator U, constructed by the successive application of the gates of the circuit. This operator can be written as a linear combination of the elements of the Pauli space $\{\mathbb{1} \otimes \mathbb{1}, \mathbb{1} \otimes X, \mathbb{1} \otimes Y, \mathbb{1} \otimes Z, \ldots, X \otimes Z, Y \otimes Z, Z \otimes Z\}$. For each family of gates, we design 4000 random circuits and see how their unitaries fill the Pauli space, compared to the uniform distribution. Since the Pauli space in the two-qubit system is a 16-dimensional space, we use a dimensionality reduction technique called UMAP [34–36] to visualize the distribution in two dimensions. The details of this algorithm are provided in the Supplemental Material [33]. The results are shown in Fig. 3. We see that the $G1$ and $G2$ circuits only fill a subset of the Pauli space. Moreover, when the number of gates is small, the filling of the space is more sparse. As the number

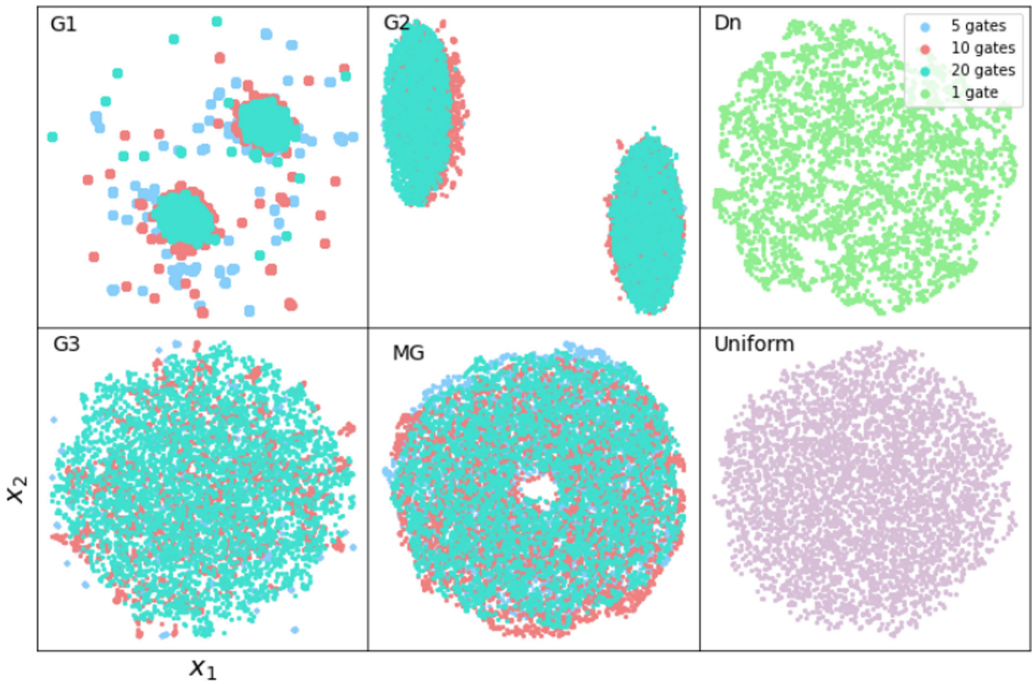

FIG. 3. Two-dimensional representation of the distribution of the families of quantum circuits in the Pauli space, compared to the uniform distribution.

of circuit gates increases, the unitaries concentrate in a dense region of the space. This fact justifies that QRs with more gates produce worse results in the QML task for these two families. On the other hand, the $G3$ family fills the Pauli space uniformly. As the number of gates increase, the distribution of the unitaries resembles more the uniform sampling. For this reason, the performance of the QR improves with the number of gates until it achieves its optimal value. The observed threshold at around 100 gates is related to the amount of them needed to start spanning the effective Pauli space of the problem in a complete way. The number of gates at which the MSE reaches an asymptotic low value can be associated to the amount of gates at which no improvement in this spanning can be achieved. Regarding the matchgate circuits, they behave similarly to the $G3$ family, except that they do not fill a small region of the Pauli space, thus leading to a slightly worse performance in the QML algorithm. Finally, the diagonal circuits (which in the two-qubit space coincide) also fill the whole Pauli space. However, there are regions with higher density than others. This also illustrates the slightly higher error in the QRC model. The SM [33] contains a short video complementing Fig. 3. In it, the number of gates of the circuit change in time. After analyzing the performance of the seven families of circuits, we can compare them with the results of the Ising model, which has been extensively used as QR [16,18–20]. Figure 2 shows that the MSE of the Ising model (with the parameters from Ref. [30]) is slightly higher than the MSE for the $G3$ family. The choice of parameters from both Refs. [20] and [30] provide very similar results, even though the parameters from Ref. [30] give a slightly better performance. Apart from its performance, we can also calculate the number of gates needed to implement the Ising model in a gate-based quantum computer. The time evolution operator $e^{-iH_{\text{Ising}}T}$ can be approximated by first-order Trotter decomposition [37]. This decomposition provides a quantum circuit with gates from the set $\{H, \text{CNOT}, R_z(\theta_i)\}_i$, where $R_z(\theta_i)$ is the rotation of an angle θ_i around the Z axis. Unfortunately, it is impossible to implement rotations with perfect accuracy in the current quantum computers. Fault-tolerant quantum computers typically perform these rotations using multiple applications of gates H and T. For this reason, we have decomposed [38] the Ising time evolution operator to a quantum circuit with gates from the set $\{H, \text{CNOT}, T\}$, which is the $G3$ family. We ran 400 simulations with the different parameters in the Ising Hamiltonian. For the LiH molecule, constructing the Ising quantum circuit required on average 11 381 gates, and 17 335 for H_2O. As shown in Fig. 2, the optimal performance of the QR for the $G3$ family is achieved with only 200 gates (250 for H_2O). Therefore, there is no need to use tens of thousands of gates to achieve optimal performance in the QR. It is worth mentioning that this comparison is only valid for gate-based quantum computers. For quantum computing based on physical systems [39] or quantum simulators [40] the transverse-field Ising model is directly implemented and it would have the complexity provided by the $G3$ family.

Conclusions. In this Letter we provide a criterion to design optimal QRs for QML. This criterion is also easy to implement in NISQ devices since it requires using circuits with only a few quantum gates. We demonstrated that the optimal circuits obtained with the prescriptions in this work need significantly less quantum gates and provide a similar, slightly better performance than the commonly used Ising model. This is of outmost importance for optimal implementations in current NISQ devices since only circuits with a few and simple gates can guarantee the required accuracy. The key point of our work is the use of the majorization principle [22] as an

indicator for the complexity of the quantum circuits. The QRs with higher complexity according to the majorization criterion provide better results in QML tasks. We also give an intuitive explanation of how the studied families of quantum circuits extract information from their initial state. We see that the optimal family of quantum circuits uniformly fills the Pauli space of operators, while the other families do not reproduce all the operators in the Pauli space. A final important remark is that the robustness of our results is expected to be ultimately related to the fidelity reached within each family of circuits, which will be also dependent on the kind of NISQ used. Hence the majorization criterion will be of relevance in a given noise strength window. The precise determination of it will be the subject of future investigations.

The code and data that support the findings of this study are openly available and can be found in Ref. [41].

Acknowledgments. The project that gave rise to these results received the support of a fellowship from "la Caixa" Foundation (ID No. 100010434). The fellowship code is LCF/BQ/DR20/11790028. This work has also been partially supported by the Spanish Ministry of Science, Innovation, and Universities, Gobierno de España, under Contracts No. PGC2018-093854-BI00 and No. ICMAT Severo Ochoa CEX2019-000904-S and by the People Programme (Marie Curie Actions) of the European Union's Horizon 2020 Research and Innovation Program under Grant No. 734557.

[1] Y. Manin, *Computable and Uncomputable* (Sovestskiye Radio Press, Moscow, 1980).

[2] R. P. Feynman, Simulating physics with computers, Int. J. Theor. Phys. **21**, 467 (1982).

[3] F. Arute, J. M. Martinis *et al.*, Quantum supremacy using a programmable superconducting processor, Nature (London) **574**, 505 (2019).

[4] A. Cho, IBM casts doubt on Google's claims of quantum supremacy, https://www.science.org/content/article/ibm-casts-doubt-googles-claims-quantum-supremacy.

[5] Y. A. Liu, X. L. Liu, F. N. Li, H. Fu, Y. Yang, J. Song, P. Zhao, Z. Wang, D. Peng, H. Chen, C. Guo, H. Huang, W. Wu, and D. Chen, Closing the "quantum supremacy" gap: Achieving real-time simulation of a random quantum circuit using a new sunway supercomputer, in *SC '21: Proceedings of the International Conference for High Performance Computing, Networking, Storage and Analysis* (Association for Computing Machinery, New York, 2021).

[6] R. Barends, J. M. Martinis *et al.*, Superconducting quantum circuits at the surface code threshold for fault-tolerance, Nature (London) **508**, 500 (2014).

[7] C. Ryan-Anderson *et al.*, Realization of Real-Time Fault-Tolerant Quantum Error Correction, Phys. Rev. X **11**, 041058 (2021).

[8] P. W. Shor, Polynomial-time algorithms for prime factorization and discrete logarithms on a quantum computer, SIAM J. Comput. **26**, 1484 (1997).

[9] L. K. Grover, A fast quantum mechanical algorithm for database search, in *Proceedings of the Twenty-Eighth Annual ACM Symposium on Theory of Computing* (Association for Computing Machinery, New York, 1996), p. 212.

[10] I. M. Georgescu, S. Ashhab, and F. Nori, Quantum simulation, Rev. Mod. Phys. **86**, 153 (2014).

[11] S. McArdle, S. Endo, A. Aspuru-Guzik, S. C. Benjamin, and X. Yuan, Quantum computational chemistry, Rev. Mod. Phys. **92**, 015003 (2020).

[12] Thematic issue on: Materials for qubits, Materials for qubits, Nat. Rev. Mater. **6**, 869 (2021).

[13] J. Preskill, Quantum computing in the NISQ era and beyond, Quantum **2**, 79 (2018).

[14] K. Bharti, A. Cervera-Lierta, T. H. Kyaw, T. Haug, S. Alperin-Lea, A. Anand, M. Degroote, H. Heimonen, J. S. Kottmann, T. Menke, W.-K. Mok, S. Sim, L. C. Kwek, and A. Aspuru-Guzik, Noisy intermediate-scale quantum algorithms, Rev. Mod. Phys. **94**, 015004 (2022).

[15] K. Fujii and K. Nakajima, Quantum reservoir computing: A reservoir approach toward quantum machine learning on near-term quantum devices, in *Reservoir Computing: Theory, Physical Implementations, and Applications*, edited by K. Nakajima and I. Fischer (Springer Singapore, Singapore, 2021), pp. 423–450.

[16] S. Ghosh, A. Opala, M. Matuszewski, T. Paterek, and T. C. H. Liew, Quantum reservoir processing, npj Quantum Inf. **5**, 35 (2019).

[17] P. Mujal, R. Martínez-Peña, J. Nokkala, J. García-Beni, G. L. Giorgi, M. C. Soriano, and R. Zambrini, Opportunities in quantum reservoir computing and extreme learning machines, Adv. Quantum Technol. **4**, 2100027 (2021).

[18] J. Chen, H. I. Nurdin, and N. Yamamoto, Temporal Information Processing on Noisy Quantum Computers, Phys. Rev. Appl. **14**, 024065 (2020).

[19] A. Kutvonen, K. Fujii, and T. Sagawa, Optimizing a quantum reservoir computer for time series prediction, Sci. Rep. **10**, 14687 (2020).

[20] H. Kawai and Y. Nakagawa, Predicting excited states from ground state wave function by supervised quantum machine learning, Mach. Learn.: Sci. Technol. **1**, 045027 (2020).

[21] J. I. Latorre and M. A. Martín-Delgado, Majorization arrow in quantum-algorithm design, Phys. Rev. A **66**, 022305 (2002).

[22] R. O. Vallejos, F. de Melo, and G. G. Carlo, Principle of majorization: Application to random quantum circuits, Phys. Rev. A **104**, 012602 (2021).

[23] J. Haferkamp, P. Faist, N. Kothakonda, J. Eisert, and N. Y. Halpern, Linear growth of quantum circuit complexity, Nature Phys. **18**, 528 (2022).

[24] A. Peruzzo, J. McClean, P. Shadbolt, M.-H. Yung, X.-Q. Zhou, P. J. Love, A. Aspuru-Guzik, and J. L. O'Brien, A variational eigenvalue solver on a photonic quantum processor, Nat. Commun. **5**, 4213 (2014).

[25] D. Gottesman, The Heisenberg representation of quantum computers, *Group22: Proceedings of the XXII International Colloquium on Group* (International, Boston, 1999).

[26] R. Jozsa and M. V. den Nest, Classical simulation complexity of extended clifford circuits, Quantum Inf. Comput. **14**, 633 (2014).

[27] R. Jozsa and A. Miyake, Matchgates and classical simulation of quantum circuits, Proc. R. Soc. A **464**, 3089 (2008).

[28] D. J. Brod and A. M. Childs, The computational power of matchgates and the xy interaction on arbitrary graphs, Quantum Inf. Comput. **14**, 901 (2014).

[29] M. J. Bremner, R. Jozsa, and D. J. Shepherd, Classical simulation of commuting quantum computations implies collapse of the polynomial hierarchy, Proc. R. Soc. A **467**, 459 (2011).

[30] R. Martínez-Peña, G. L. Giorgi, J. Nokkala, M. C. Soriano, and R. Zambrini, Dynamical Phase Transitions in Quantum Reservoir Computing, Phys. Rev. Lett. **127**, 100502 (2021).

[31] Y. Cao, J. Romero, J. P. Olson, M. Degroote, P. D. Johnson, M. Kieferová, I. D. Kivlichan, T. Menke, B. Peropadre, N. P. D. Sawaya, S. Sim, L. Veis, and A. Aspuru-Guzik, Quantum chemistry in the age of quantum computing, Chem. Rev. **119**, 10856 (2019).

[32] P. Jordan and E. Wigner, Über das paulische äquivalenzverbot, Z. Phys. **47**, 631 (1928).

[33] See Supplemental Material at http://link.aps.org/supplemental/10.1103/PhysRevE.106.L043301 for Optimal quantum reservoir computing for the NISQ era.

[34] L. McInnes, J. Healy, and J. Melville, UMAP: uniform manifold approximation and projection for dimension reduction, arXiv:1802.03426.

[35] A. Coenen and A. Pearce, Understanding UMAP, https://paircode.github.io/understanding-umap/ (2020-04-09).

[36] L. van der Maaten and G. Hinton, Visualizing data using t-SNE, J. Mach. Learn. Res. **9**, 2579 (2008).

[37] J. D. Whitfield, J. Biamonte, and A. Aspuru-Guzik, Simulation of electronic structure Hamiltonians using quantum computers, Mol. Phys. **109**, 735 (2011).

[38] N. J. Ross, Optimal ancilla-free CLIFFORD+V approximation of z-rotations, Quantum Inf. Comput. **15**, 932 (2015).

[39] J. Smith, A. Lee, P. Richerme, B. Neyenhuis, P. W. Hess, P. Hauke, M. Heyl, D. Huse, and C. Monroe, Many-body localization in a quantum simulator with programmable random disorder, Nature Phys. **12**, 907 (2016).

[40] J. Zhang, G. Pagano, P. W. Hess, A. Kyprianidis, P. Becker, H. B. Kaplan, A. V. Gorshkov, Z.-X. Gong, and C. R. Monroe, Observation of a many-body dynamical phase transition with a 53-qubit quantum simulator, Nature (London) **551**, 601 (2017).

[41] Code and Data supporting this study can be found in: https://github.com/laiadc/Optimal_QRC.